Electronic Research Archive

ERA, 33(9): 5231–5251.
DOI: 10.3934/era.2025234
Received: 18 June 2025
Revised: 01 August 2025
Accepted: 13 August 2025
Published: 04 September 2025

https://www.aimspress.com/journal/ERA

Research article

Influence of obstacle configuration on electrolyte flow in serpentine flow fields for redox flow batteries

Joseba Martínez-López[1], Koldo Portal-Porras[1], Unai Fernández-Gamiz[1,*], Eduardo Sánchez-Díez[2], Aitor Beloki-Arrondo[3] and Íñigo Ortega-Fernández[3]

[1] Nuclear Engineering and Fluid Mechanics Department, University of the Basque Country UPV/EHU, Nieves Cano 12, Vitoria-Gasteiz 01006, Spain
[2] Centre for Cooperative Research on Alternative Energies (CIC EnergiGUNE), Basque Research and Technology Alliance (BRTA), Alava Technology Park, Albert Einstein 48, Vitoria-Gasteiz 01510, Spain
[3] TECNALIA Research & Innovation, Basque Research and Technology Alliance (BRTA), Mikeletegi Pasealekua 2, Donostia-San Sebastian 20009, Spain

* **Correspondence:** Email: unai.fernandez@ehu.eus.

Abstract: In this study, a three-dimensional numerical model was developed to investigate the influence of obstacles on the hydrodynamic behavior of a serpentine flow field. Various obstacle geometries (rectangular, trapezoidal, triangular, and cylindrical), quantities (1–3 blocks), and positions (straight vs. curved channel sections) were systematically analyzed. Results show that rectangular obstacles enhance mean velocity but significantly increase pressure drop and reduce flow uniformity. In contrast, trapezoidal and cylindrical shapes offer a more balanced tradeoff, achieving improved uniformity and flow enhancement with moderate hydraulic penalties. Increasing obstacle number improves electrolyte velocity uniformity across all cases, though diminishing returns are observed beyond two blocks. Importantly, placing obstacles in curved sections of the serpentine field yields up to 9% higher uniformity compared to straight placements, without increasing pressure loss—leveraging pre-existing low-velocity regions to enhance distribution. These findings align with previous literature and highlight that optimized obstacle shape, number, and positioning can significantly improve mass transport and flow distribution in vanadium redox flow batteries (VRFBs). To complement the computational fluid dynamics (CFD) analysis, an artificial neural network (ANN) was trained to predict pressure drop using key geometric and flow features as inputs. The ANN demonstrated excellent agreement with numerical results and reduced the computational time required to obtain the results by 6 orders of magnitude.

Keywords: vanadium redox flow battery; flow field; obstruction; numerical model; serpentine; pressure drop

1. Introduction

Increasing integration of renewable energy sources has intensified the demand for scalable, efficient, and responsive energy storage systems. Lowering the dependence on fossil fuels and transitioning to clean energy sources like solar and wind poses problems like inherent intermittency and variability [1,2]. Therefore, energy storage systems are required to offer stability and reliability to the power grid to achieve renewable energy integration [3].

Redox flow batteries (RFBs) have gradually gained attention from the research community in the energy storage landscape, particularly for applications requiring high cyclability and long duration [4]. This technology offers a distinct advantage: the separation of energy capacity from power output [5]. This decoupled configuration makes RFBs flexible in terms of design, enabling tailored solutions for different demands. Among the various chemistries explored for RFBs, vanadium redox flow batteries (VRFBs) stand as one of the most widely studied and commercially available [6,7]. Its appeal lies in the use of vanadium ions in four oxidation states as both the positive and negative active species, which eliminates the issue of cross-contamination between half-cells [8]. However, one of the primary challenges is the relatively low energy density, stemming from the solubility limit of vanadium species [9,10]. In addition, other key components like electrodes and membranes increase the capital costs of this technology.

One approach to improve performance without significantly increasing system costs lies in the optimization of flow field design [11,12]. By tailoring the geometry of the electrolyte distribution channels, it is possible to improve mass transport, enhance reactant utilization, and reduce local concentration gradients—thereby increasing overall electrochemical efficiency without modifying core materials or introducing expensive components [13,14]. The most commonly employed configurations include flow-through (without a structured flow field) and flow-by architectures such as serpentine (SFF), interdigitated (IFF), and parallel (PFF) [11,15]. At high gross power conditions, Messaggi et al. [16] showed that the SFF configuration achieved higher net efficiency than IFF, although the reverse behavior was observed under low power conditions. Xu et al. [17] concluded that serpentine flow fields obtained higher energy and round-trip efficiency than parallel flow fields by means of a three-dimensional numerical model. In this line, Maurya et al. [11] demonstrated that IFF fails to maintain performance at higher current densities due to limited convective transport, even at elevated flow rates. Wang et al. [18] showed that the SFF induces stronger convective flow, resulting in improved mass transfer compared to the interdigitated configuration.

In addition to the overall flow field configuration, the geometric characteristics of channel sections play a crucial role. Recent studies have highlighted the potential of modifying dimensions such as width or cross-sectional shape to enhance cell performance. Yue et al. [19] proposed a trapezoidal flow field, which significantly enhanced voltage efficiency and electrolyte utilization by improving mass transport. Lee et al. [20] employed a three-dimensional numerical model to investigate the effects of channel size and electrolyte flow rate for the serpentine configuration. Results demonstrated that reduced channel dimensions and higher flow rates enhanced electrochemical performance caused by the improved distribution of active species, albeit at the cost of increased

pressure drop across the cell. Ali et al. [21] examined serpentine and staggered configurations with channel widths of 2 and 5 mm, revealing that narrower channels resulted in higher discharge voltage and more uniform distribution of active species. In contrast, Gundlapalli and Jayanti [22] concluded that widening the channels can help reduce pressure drop while maintaining electrochemical activity for serpentine cells. Sun et al. [23] studied the effects of changing the rib width for the serpentine configuration. The limiting current density was increased by 60% with the modified design, compared to the conventional serpentine flow field. Energy efficiency increased by 4% along with electrolyte penetration uniformity. Guo et al. [24] numerically modeled a convection-enhanced serpentine flow field. Higher uniformity of reactant distribution was achieved with increasing channel number and decreasing channel fraction. However, the pumping work was increased. A novel spiral flow field was investigated by Huang et al. [25] by means of a numerical model. Compared to a serpentine and parallel flow field, the spiral flow field reduced local concentration polarization; however, this improvement was accompanied by increased pressure drop and diminished overall system efficiency. Pan et al. [26] linearly reduced the channel depth from inlet to outlet in a conventional serpentine flow field. Numerical simulations revealed that a gradient of 25% led to the highest pump-based voltage efficiency. The application of this design on an experimental setup demonstrated an increase in electrolyte utilization and energy efficiency for low flow rates and high current density. Wang et al. [13] tested the experimental performance of a trapezoidal runner cross-section against the conventional rectangular cross-section serpentine flow field. Pump power-based voltage efficiency, discharge voltage, and energy efficiency were observed to improve with the trapezoidal cross-section. Ramesh et al. [14] proposed a convergent-divergent flow field (CDFF) to enhance cell efficiency while reducing pressure drop. Peak power density was increased by 12% and a 100 mV average reduction in polarization for 100 mA cm^{-2} was achieved compared to SFF, while a lower pressure drop was obtained.

The introduction of obstacles has been studied by some authors. Akuzum et al. [27] introduced ramps and prismatic obstructions in IFF and SFF and compared the results to conventional flow fields. Lower pressure drops were obtained with obstruction placement relative to the baseline flow fields. However, due to electrolyte bypassing, no performance improvements were observed. Messaggi et al. [28] studied the effects of introducing one obstruction located at the channel wall and another one near the electrode interface with a 3D numerical model. Better electrolyte penetration through the electrode was obtained with both obstructions, but the second one close to the electrode offered better balance between electrochemical performance, pressure drop, and capacity. Liu et al. [29] investigated the influence of obstacle shape within biomimetic flow fields. The highest concentration uniformity and discharge voltage, and the lowest charge voltage, were obtained with circular obstacles. Martínez-López et al. [30] examined the impact of obstruction placement in a flow-through configuration against a baseline design. Improvements in concentration uniformity, minimum concentration, and limiting current density were observed, more significantly at lower flow rates. However, pressure drop increased, indicating a tradeoff between hydraulic and electrochemical performance.

Although obstacle-based modifications to flow fields have been previously investigated, the present study distinguishes itself by providing a systematic and comparative analysis of multiple design variables—including obstacle geometry (rectangular, trapezoidal, triangular, and cylindrical), number (from one to three), and positioning (in straight versus curved segments of the serpentine channel). To the best of our knowledge, no prior work has jointly assessed the combined effects of these three factors on the hydrodynamic behavior of redox flow batteries. Most existing studies tend to explore a single obstacle shape or configuration, without offering a structured framework for

comparing their influence on flow uniformity, pressure drop, and electrode utilization.

2. Materials and methods

2.1. Model description

2.1.1. Fundamental principles

Figure 1 illustrates the basic architecture of the vanadium redox flow battery. The system incorporates two independent electrolyte reservoirs: the positive one stores VO^{2+} and VO_2^+, and the negative contains V^{2+} and V^{3+}. Peristaltic pumps are in charge of pumping the electrolytes through the flow fields to the porous electrodes, where the electrochemical reactions occur. To electrically insulate both electrodes, an ion-selective membrane is placed, which allows certain ions to pass through while preventing cross-contamination. Equations (1) and (2) show the reactions in the positive and negative electrodes, respectively.

$$VO_2^+ + 2H^+ + e^- \rightleftharpoons VO^{2+} + H_2O \tag{1}$$

$$V^{3+} + e^- \rightleftharpoons V^{2+} \tag{2}$$

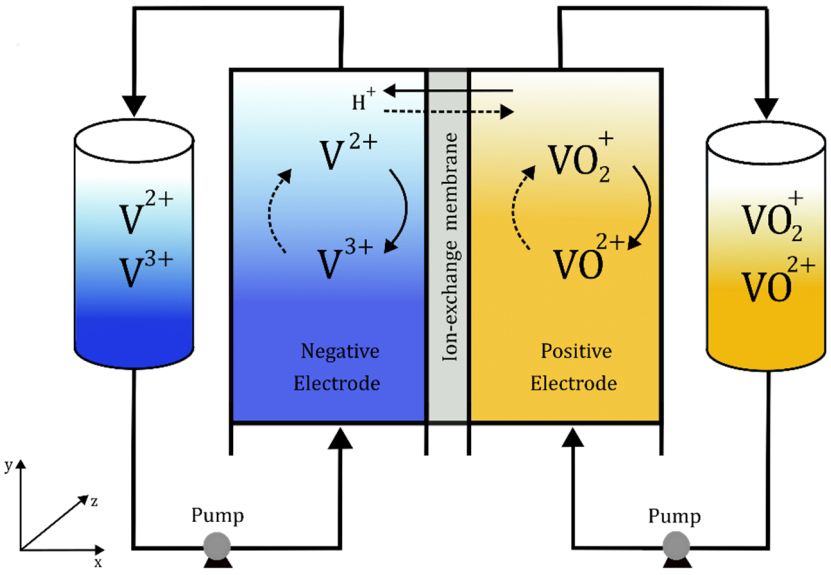

Figure 1. Schematic representation of a vanadium redox flow battery.

The model developed in this study represents a three-dimensional half-cell. Two domains are modeled: the flow field and the electrode. The following assumptions are taken into consideration for the numerical model:

- The flow field, electrolyte, and electrode properties are isotropic.
- The model is analyzed under steady-state conditions.
- The electrolyte is treated as incompressible.
- A fully developed flow is assumed at the inlet.
- A laminar flow is assumed.

2.1.2. Governing equations

The electrolyte transport through the porous electrode was modeled using the Brinkman equations, appropriate for this scenario. This formulation captures the transition between free flow and flow within porous media by incorporating elements of both Darcy's law and Navier-Stokes equations, presented in Eqs (3)–(7). For flow fields, the governing equations are:

$$\rho(\mathbf{u}\cdot\nabla)\mathbf{u} = \nabla\cdot[-\mathrm{p}\mathbf{I}+\mathbf{K}]+\boldsymbol{F} \tag{3}$$

$$\rho\nabla\cdot\mathbf{u} = 0 \tag{4}$$

where ρ is electrolyte density, $\mathbf{u}$ indicates electrolyte velocity, p stands for pressure, $\mathbf{K}$ refers to stress tensor, and $\boldsymbol{F}$ indicates volume forces. For the porous electrode:

$$\frac{1}{\varepsilon_p}\rho(\mathbf{u}\cdot\nabla)\mathbf{u}\frac{1}{\varepsilon_p} = \nabla\cdot[-\mathrm{p}\mathbf{I}+\mathbf{K}]-\left(\mu k^{-1}+\beta\rho|\mathbf{u}|+\frac{Q}{\varepsilon_p^2}\right)\mathbf{u}+\boldsymbol{F} \tag{5}$$

$$\rho\nabla\cdot\mathbf{u} = \mathrm{Q} \tag{6}$$

$$\mathbf{K} = \mu\frac{1}{\varepsilon_p}(\nabla\mathbf{u}+(\nabla\mathbf{u})^T)-\frac{2}{3}\mu\frac{1}{\varepsilon_p}(\mathbf{u}\cdot\nabla)\mathbf{I} \tag{7}$$

where ε_p refers to electrode porosity, μ stands for electrolyte dynamic viscosity, Q is the source term for mass sources or sinks, k refers to electrode permeability, and β is a nonlinear parameter.

2.1.3. Boundary condition

To define the flow behavior, no-slip conditions were applied along the walls of both the free-flow channel and the porous electrode region. At the interface between the porous electrode and the flow channel, a slip condition was introduced. The inlet boundary was prescribed with a flow velocity based on Reynolds number regime, while the outlet was constrained by a pressure boundary condition set to 0 Pa.

2.1.4. Battery performance parameter

An essential parameter for assessing the spatial distribution of flow within the system is the uniformity factor. This metric provides a quantitative measure of how evenly velocity is distributed across a given domain:

$$U_i = 1-\frac{1}{u_{avg}}\sqrt{\frac{1}{V}\iiint\left(u-u_{avg}\right)^2 dV} \tag{8}$$

where u_{avg} refers to the average velocity, and V stands for electrode volume.

2.2. Numerical model

The numerical model was implemented using COMSOL Multiphysics 5.5. The Free and Porous Media Flow module was employed. It applies the Brinkman equations for slow flow in a porous electrode and the Navier-Stokes equations for flow fields. The finite volume method was used to obtain the numerical solution. The PARDISO solver was utilized, applying a relative error tolerance of $1\cdot$

10^{-6} to ensure numerical accuracy. A mesh independence study was conducted to balance computational efficiency and solution fidelity, revealing that further refinement beyond 1,880,796 elements resulted in negligible changes, as illustrated in Figure 2.

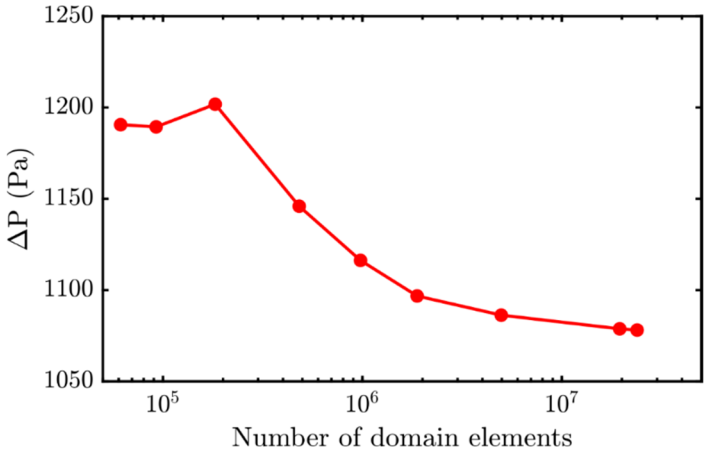

Figure 2. Results of the mesh independence study.

3. Results

3.1. Experimental validation

The three-dimensional model has been validated with experimental data from Wang et al. [31], for a 4 cm × 4 cm VRFB featuring a serpentine flow field with 2 mm × 2 mm channels. Three different electrode compression ratios were analyzed: 14.16%, 41.83%, and 69.57%.

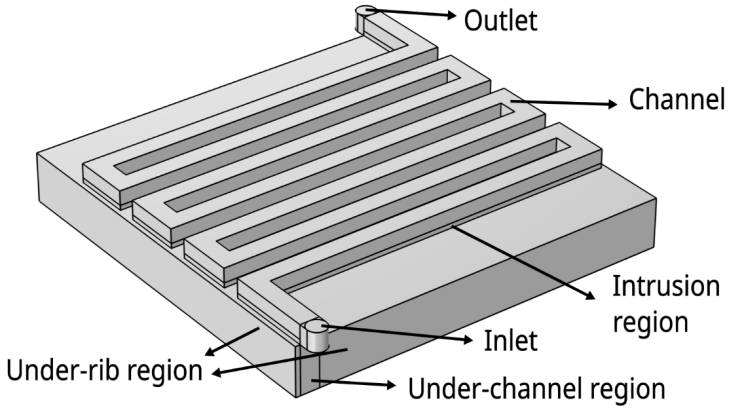

Figure 3. Three-dimensional numerical model with serpentine flow field and the different sub-regions when applying electrode compression.

To account for the inhomogeneous deformation of the electrode caused by the channel-rib pattern,

which affects physical properties such as permeability and porosity, electrode thickness, and the height of the electrode intrusion into the channel, the electrode is divided into three sub-regions: the intrusion region, the under-channel region, and the under-rib region (see Figure 3).

The geometric, porosity, and permeability values for each sub-region at different compression ratios taken from [31] are provided in Table 1.

Table 1. Geometric dimensions and electrode properties for different electrode compression ratios.

	CR = 14.16%	CR = 41.83%	CR = 69.57%
Porous electrode thickness	5.15 mm	3.49 mm	1.83 mm
Intrusion electrode thickness	0.51 mm	0.8 mm	1.25 mm
Flow channel height	1.49 mm	1.2 mm	0.75 mm
Rib region porosity	0.81	0.76	0.66
Channel region porosity	0.84	0.8	0.75
Intrusion region porosity	0.86	0.84	0.79
Rib region permeability	$4.38 \times 10^{-10}\,m^2$	$2.15 \times 10^{-10}\,m^2$	$7.14 \times 10^{-10}\,m^2$
Channel region permeability	$6.23 \times 10^{-10}\,m^2$	$3.61 \times 10^{-10}\,m^2$	$1.66 \times 10^{-10}\,m^2$
Intrusion region permeability	$1.08 \times 10^{-9}\,m^2$	$7.19 \times 10^{-10}\,m^2$	$3.16 \times 10^{-10}\,m^2$

The fluid used for the experiments is water at ambient temperature [31], and its properties are listed in Table 2.

Table 2. Fluid properties.

Parameter	Value
Dynamic viscosity	$1.002 \times 10^{-3}\ Pa \cdot s$
Density	$998.2\ kg \cdot m^{-3}$

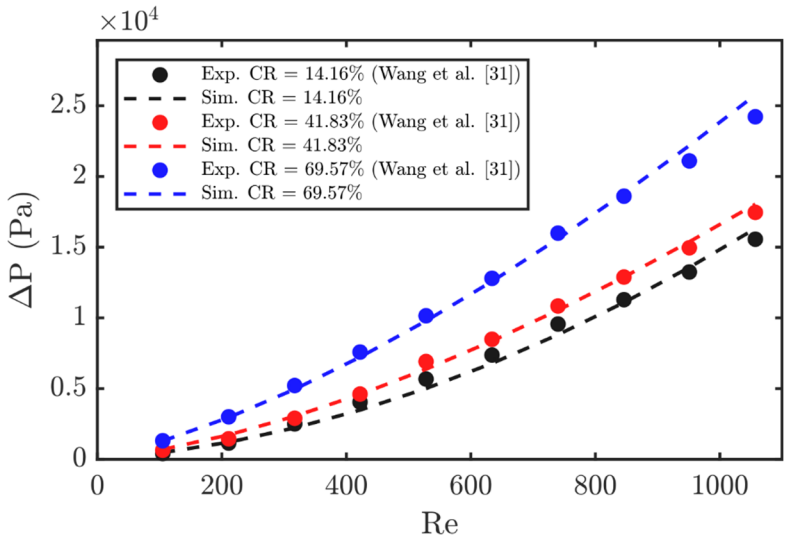

Figure 4. Comparison of numerical and experimental results [31] for pressure drop for three different electrode compression ratios.

Figure 4 shows the results of the experimental validation of the numerical model under three different electrode compression levels: 14.16%, 41.83%, and 69.57%. The average error across three compression ratios was 4.9%, confirming that the model provides a good approximation of the fluid dynamic behavior.

3.2. Case studies

The study investigates 6 configurations. The first case, referred to as *Base*, serves as the benchmark and represents an unobstructed channel without any internal structures. Four additional cases introduce different obstacle geometries positioned within the channel. The *Rect* case consists of a rectangular prism. Both *Trap-A* and *Trap-B* configurations employ a trapezoidal prism with different dimensions. The *Tri* case features a triangular prism, and the *Cyl* case includes a cylinder cut in half. All obstacles and their dimensions are illustrated in Figure 5a). In this study, blocks were inserted into the straight sections of the flow channels, as can be seen in Figure 5b).

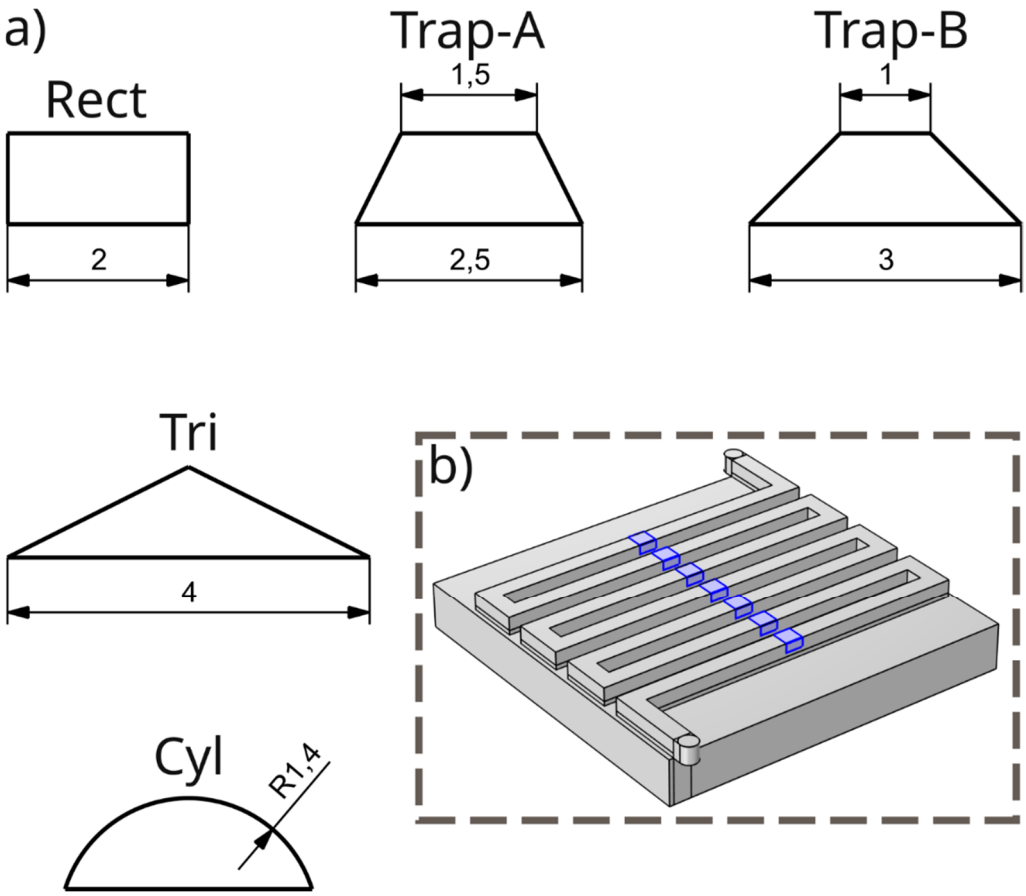

Figure 5. a) Schematic representation of all obstacles and their geometric dimensions, and b) obstacle positioning within the channels.

3.3. Block shape

Figure 6 presents the pressure drop over the half-cell for various obstacle geometries inserted in

the straight sections of the serpentine channel. *Rect* geometry exhibited the highest pressure drop, achieving approximately 56.8 kPa at Re = 1000, a value over 4 times the *Base* case (13.7 kPa). This is attributed to the bluff nature of the Rect geometry, which generates flow separation and recirculation regions. On the other hand, *Tri* and *Cyl* geometries yielded considerably smaller pressure drops, with *Cyl* reaching 39 kPa, a reduction of about 31% compared to *Rect*. The trapezoidal geometries (*Trap-A* and *Trap-B*) exhibited intermediate values, with *Trap-B* giving marginally lower values.

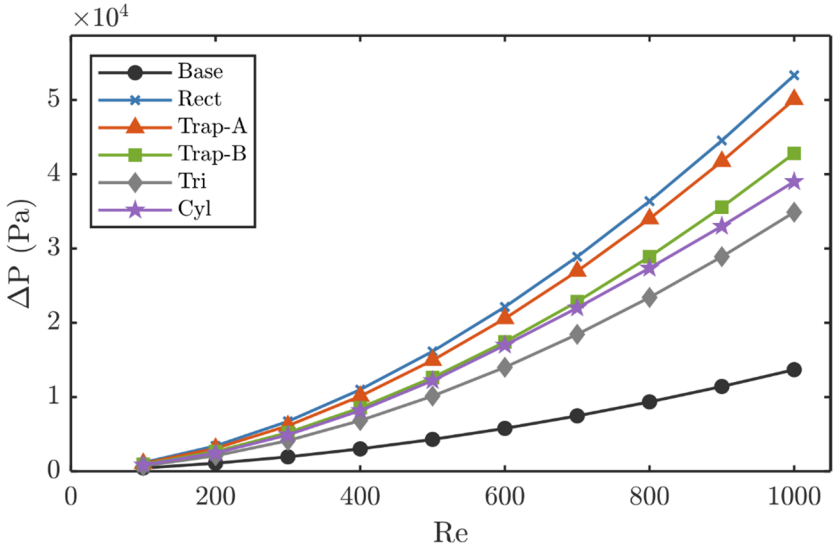

Figure 6. Pressure drop obtained with different obstacle shapes.

The influence of obstacle shape on the uniformity of electrolyte velocity in the porous electrode domain is displayed in Figure 7a). The *Base* case performed the best with the maximum uniformity of approximately 0.284 at Re = 100, which served as the reference case. Among all the block shapes inserted, *Tri* and *Cyl* performed relatively high in terms of uniformity, with *Tri* having a 15% lower value compared to *Base* at Re = 100. The lowest was *Rect* (0.2), a 29% lower value compared to *Base*. The reduction observed is attributed to localized acceleration taking place near the blunt obstacles. At lower Reynolds numbers, *Trap-A* and *Trap-B* have lower uniformity indices than both *Tri* and *Cyl*. As the Reynolds number increases, both trapezoidal arrangements show improvements and eventually surpass the performance of the *Cyl* arrangement. Notably, at higher Reynolds numbers, *Trap-A* performs better than *Trap-B*, meaning that the more acute trapezoidal profile allows for a more effective distribution at higher flow rates. Figure 7b) illustrates the average electrolyte velocity in the electrode. In contrast to the trend toward homogeneity, the *Base* case features the lowest mean velocity ($1.97 \cdot 10^{-4}$ m/s), which is due to the lack of obstacles. The *Rect* case presents the highest values of velocity ($8.9 \cdot 10^{-4}$ m/s), which are over four times higher than those of the *Base* case. *Trap-A* and *Trap-B* show increased mean velocity up to $8 \cdot 10^{-4}$ m/s. The *Cyl* arrangement exhibited values in good accordance with *Trap-B*, especially for high Reynolds numbers, suggesting a similar efficiency in facilitating flow with minimal flow resistance. In contrast, the *Tri* shape yielded the smallest increase among the blocked shapes and exhibited a mean velocity of approximately $5.8 \cdot 10^{-4}$ m/s when Re = 1000.

Figure 7c) displays the velocity streamlines corresponding to different obstacle shapes at Re = 400. The distribution highlights the localized recirculation and high-velocity zones induced by blunt geometries such as *Rect*, while streamlined profiles such as *Cyl* and *Tri* promote smoother transitions

and reduced stagnation. These visual results confirm the quantitative trends observed in Figure 7a),b).

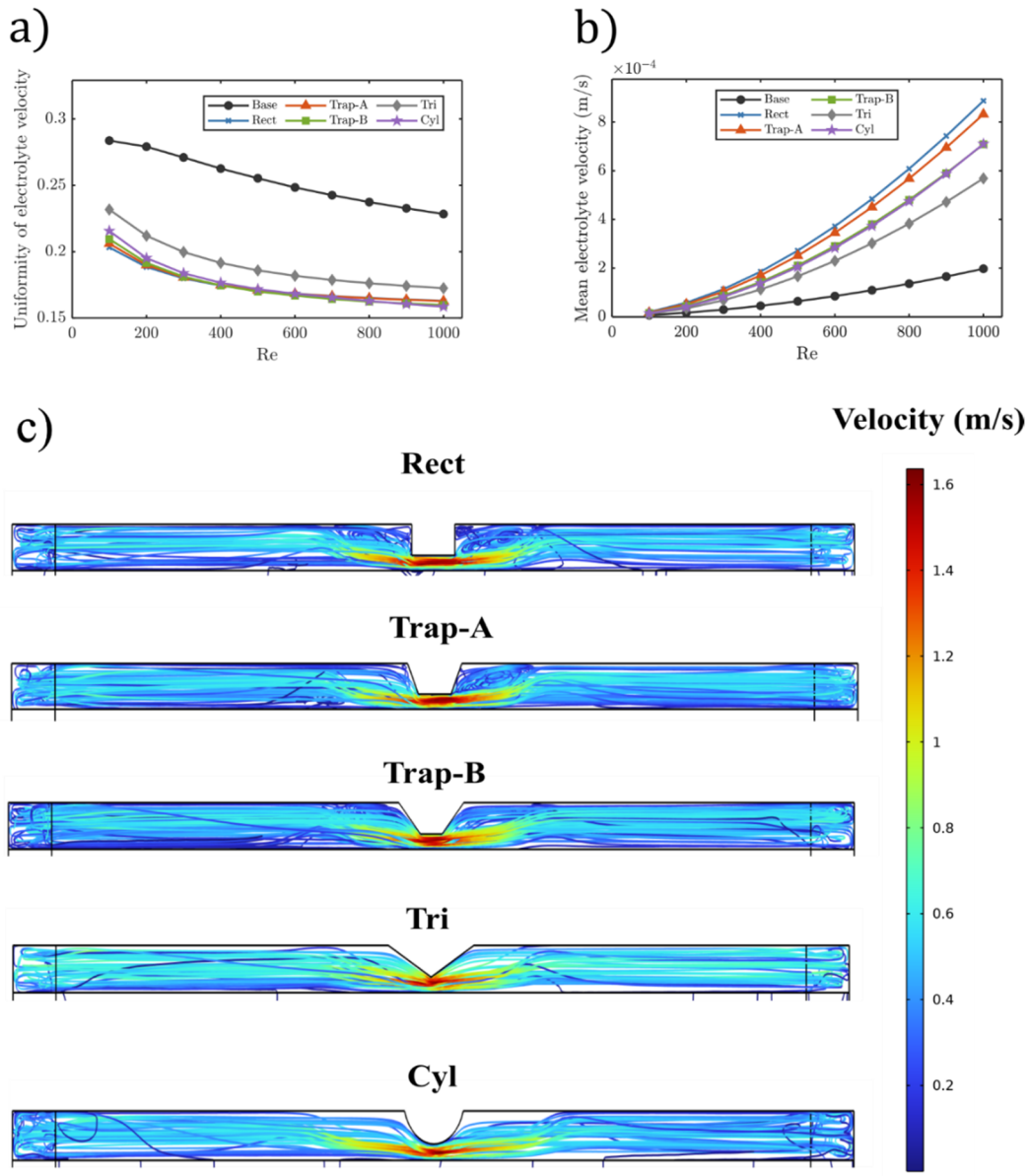

Figure 7. a) Uniformity of electrolyte velocity in the electrode, b) mean electrolyte velocity in the electrode, and c) streamlines of the electrolyte velocity for different obstacle shapes for Re = 400.

The connection between the three-dimensional velocity fields and the calculated uniformity index is direct and physically meaningful. Regions exhibiting strong recirculation or localized stagnation—typically observed near blunt obstacle geometries such as *Rect*—result in a broader velocity distribution and hence lower uniformity values. In contrast, configurations like *Trap-B* and *Tri* promote smoother and more spatially consistent flow, leading to a narrower distribution of velocities and consequently higher uniformity indices. These visual and quantitative trends are consistent across the cases presented in Figure 7a),c). These results highlight a fundamental tradeoff: while *Rect* blocks maximize electrolyte penetration and increase mean flow through the porous electrode, they do so at

the cost of significantly reduced uniformity and recirculation. *Tri* and *Cyl* geometries, on the other hand, offer a more balanced compromise between distribution and efficiency, preserving uniformity while imposing moderate hydraulic penalties.

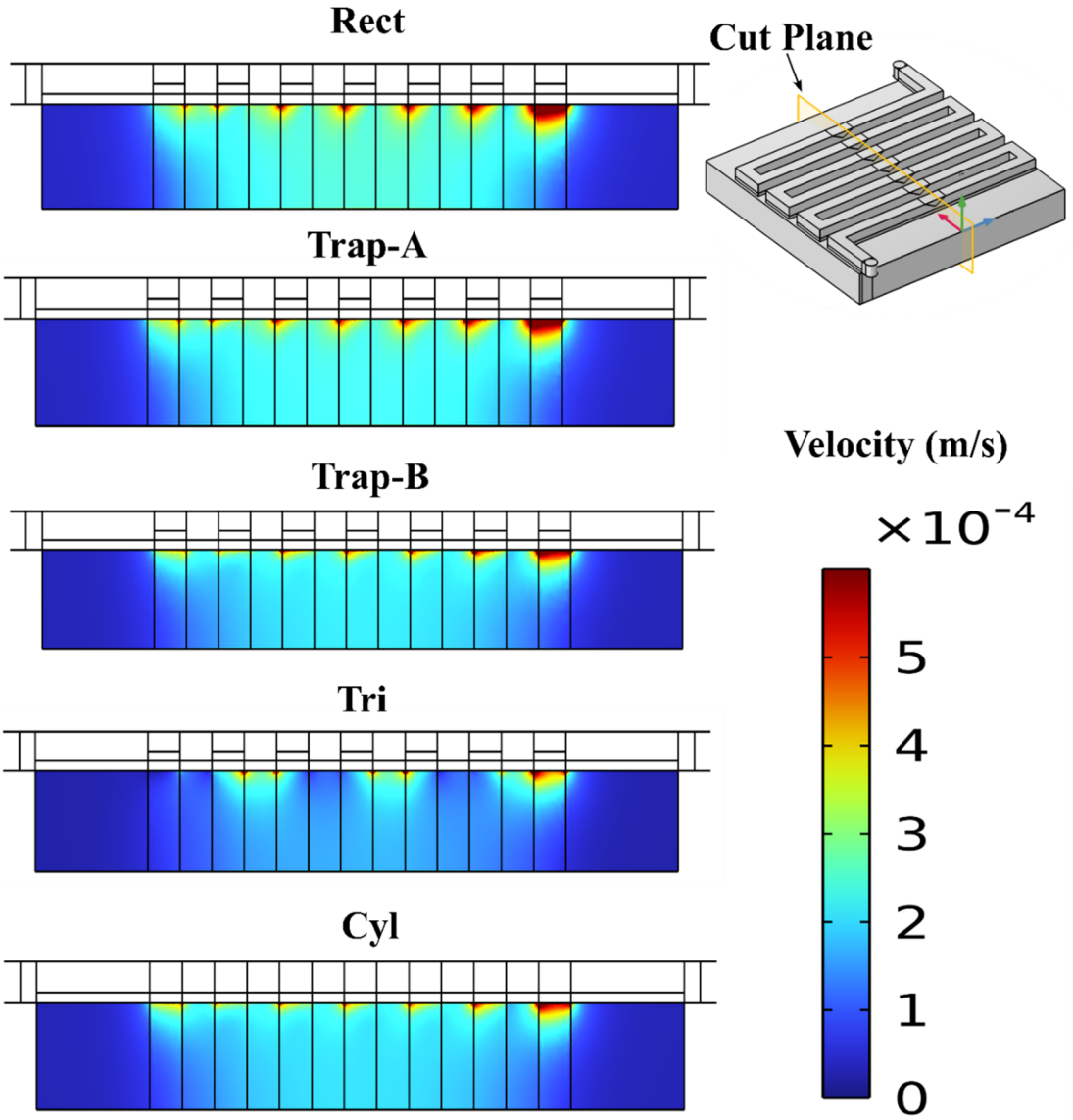

Figure 8. Velocity fields in the porous electrodes for different block shapes for Re = 400.

To better understand the influence of obstacle geometry on the electrolyte flow within the porous electrode, Figure 8 presents velocity magnitude distributions along a plane cut to analyze flow under the rib. The *Rect* configuration exhibits sharp, localized peaks of velocity beneath the rib regions, indicating strong infiltration into the porous electrode. *Trap-A* presents a slightly smoother profile, and *Trap-B* further reduces these peaks. In contrast, the *Tri* and *Cyl* geometries show significantly reduced under-rib convection, with the shallowest velocity penetration into the porous electrode. This behavior aligns with the lower average velocities observed in Figure 7b) for these shapes and higher uniformity indices in Figure 7a), suggesting that while they promote more homogeneous flow, they induce less aggressive penetration beneath the ribs.

3.4. Block number

The influence of obstacle number was investigated by incrementally increasing the quantity of blocks placed in the channel: 1, 2, and 3 per channel section. Figure 9 displays the corresponding pressure drop results. As expected, pressure loss increased in all cases due to accumulated flow obstruction. The *Rect* configuration showed the steepest rise, with pressure increasing from 11.7 kPa for 1 block to 18 kPa for 2 blocks and 24 kPa for 3 blocks. Notably, the pressure drop for *Trap-B* at three blocks is comparable to that of *Trap-A* with two blocks, indicating that *Trap-B* maintains lower hydraulic losses even at higher obstacle densities. Both *Tri* and *Cyl* maintained the lowest pressure increases among all blocked cases, reaching around 13 kPa for 3 obstacles, almost half of the *Rect* at the same obstacle number.

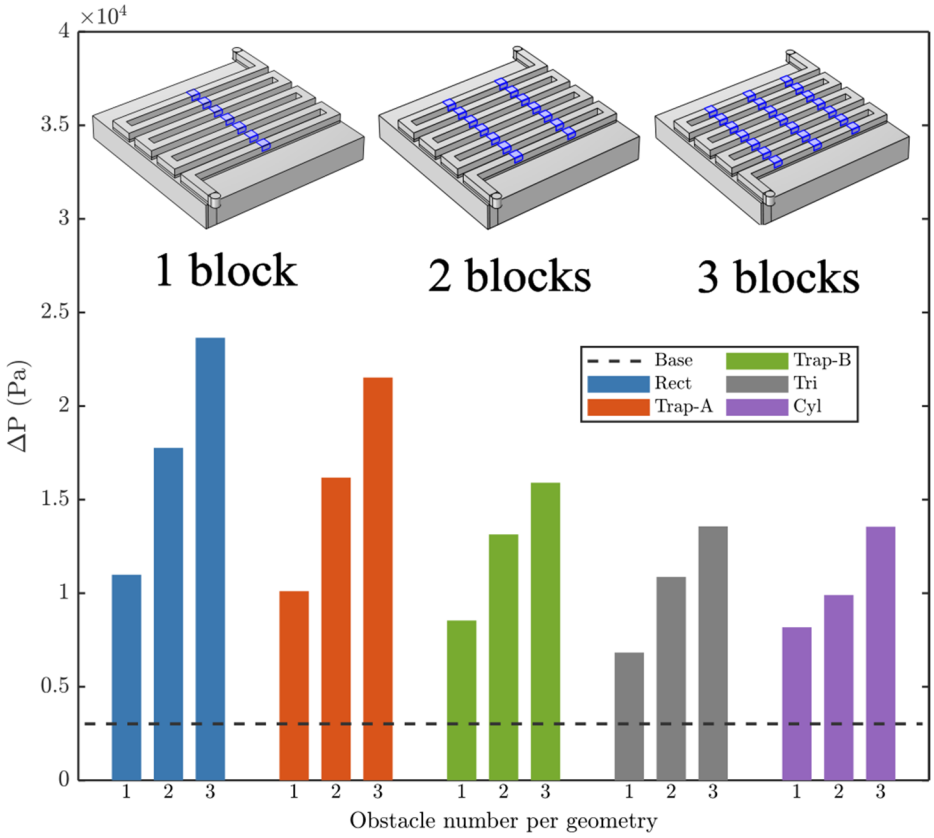

Figure 9. Pressure drop obtained for different obstacle numbers for Re = 400.

As shown in Figure 10a), the uniformity of electrolyte velocity benefited significantly from increasing the number of obstacles for all cases. For instance, in the *Rect* configuration, the uniformity index improved from 0.175 for 1 block to 0.239 when 3 blocks are placed, reducing the gap with the *Base* case. Similarly, *Trap-A* improved from 0.175 to 0.237, and *Trap-B* from 0.175 to 0.235, nearly reaching parity with the *Base*. The *Tri* and *Cyl* geometries also improved, though *Tri* did it with a smaller margin, as its initial uniformity was already high. However, the gain in uniformity between 2 and 3 blocks was markedly smaller than that from 1 to 2 blocks across all geometries, indicating diminishing returns in uniformity enhancement at higher obstacle densities. In Figure 10b), the effect of obstacle number on mean velocity is presented. Contrary to hydraulic resistance predictions, the

average electrolyte velocity was observed to rise when obstacles were introduced in all geometries. The apparently counterintuitive behavior can be attributed to improved flow redistribution and reduced stagnant regions due to enhanced channeling effects between obstacles.

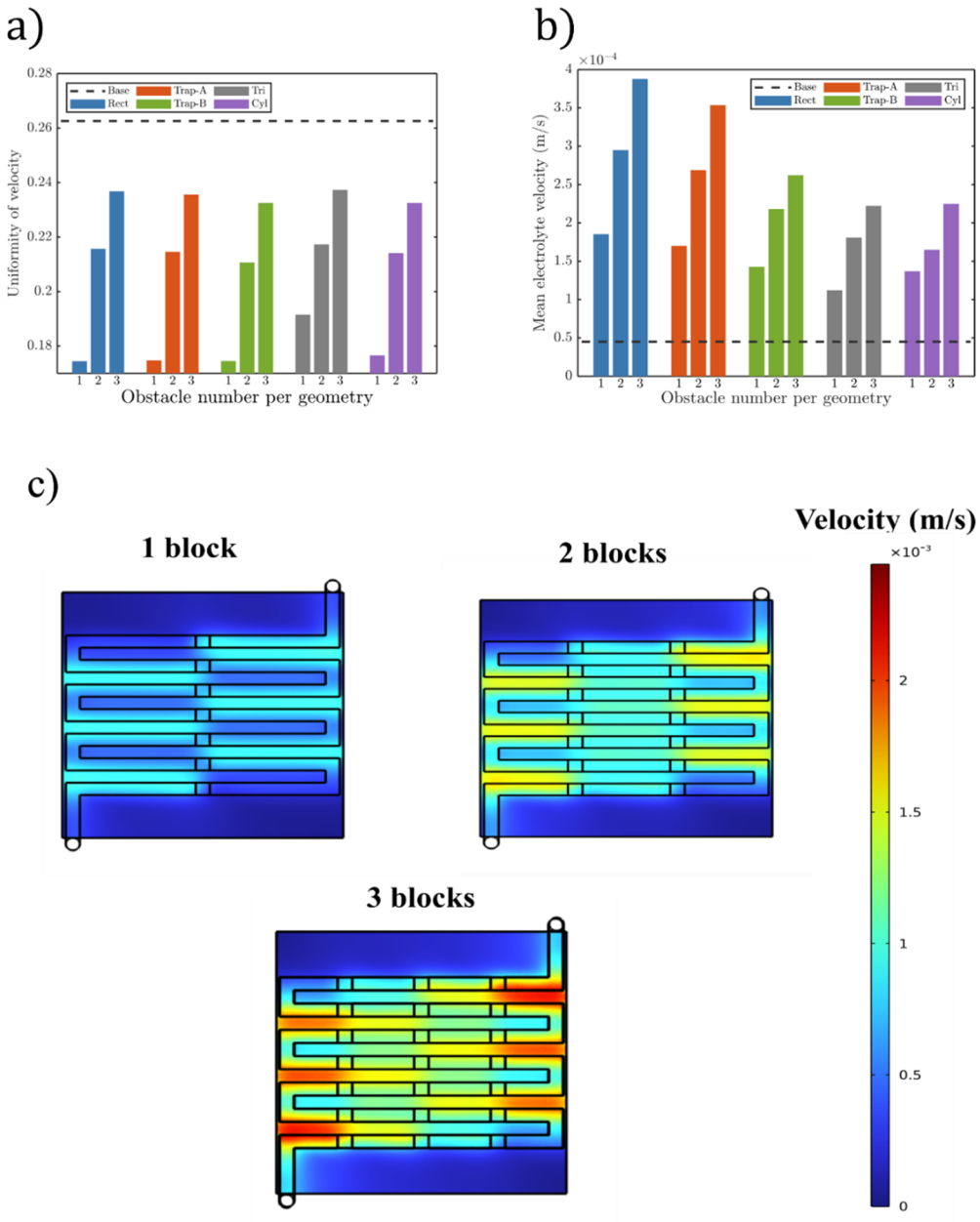

Figure 10. a) Uniformity of electrolyte velocity in the electrode, b) mean electrolyte velocity in the electrode, and c) velocity fields for different obstacle numbers for Re = 400.

The magnitude of velocity, however, varied significantly depending on the geometry. For the *Rect* configuration, mean velocity rose from approximately $1.8 \cdot 10^{-4}$ m/s (1 block) to $3.9 \cdot 10^{-4}$ m/s (3 blocks), representing a 117% increase. *Trap-B* showed a more moderate rise, from $1.45 \cdot 10^{-4}$ to $2.55 \cdot 10^{-4}$ m/s, amounting to a 76% increase. Note that *Trap-A*, with two blocks, achieved almost the same average velocity as *Trap-B*, with three blocks. In contrast, the *Cyl* configuration exhibited only a slight increase,

from $1.35 \cdot 10^{-4}$ to $2.2 \cdot 10^{-4}$ m/s. *Cyl* did not get much from additional obstacles, which is reasonable given that the streamlined design of this shape already led to the low-stagnant block count. Although all studied geometries resulted in higher average velocities as more blocks were introduced, the returns on 3 elements were particularly unnoticeable, especially for efficient shapes, such as *Cyl*, *Tri*, and *Trap-B*. Figure 10c) illustrates the velocity field distribution as the number of obstacles increases from 1 to 3 for the *Rect* case. As is evident, the addition of obstacles effectively breaks up stagnant regions and promotes more uniform electrolyte distribution, consistent with Figure 9a).

3.5. Block positioning

To evaluate the influence of block placement, two positions within the serpentine channel were compared: the previously studied straight section and the curved section. The rectangular obstacle was employed for both positions, with *Rect* referring to the straight section position and *Rect** to the curved section. As shown in Figure 11, the pressure drop varied marginally between the two placements. However, velocity uniformity exhibited more notable variations. Looking at Figure 12a), relocating the obstacles from the straight to the curved section resulted in a 9% improvement over the *Base* case, maintaining higher values when working at high Re. This behavior is consistent with the findings of Lu et al. [32], who demonstrated that inserting blocks at the bends of a serpentine flow field significantly improved species transport by homogenizing the velocity distribution. Their 3D model showed that bend-placed blocks enhanced flow uniformity. Regarding mean electrolyte velocity, illustrated in Figure 12b), the difference is modest. These results indicate that obstacles placed in curved sections leverage the already existing low-velocity zones to achieve greater flow uniformity.

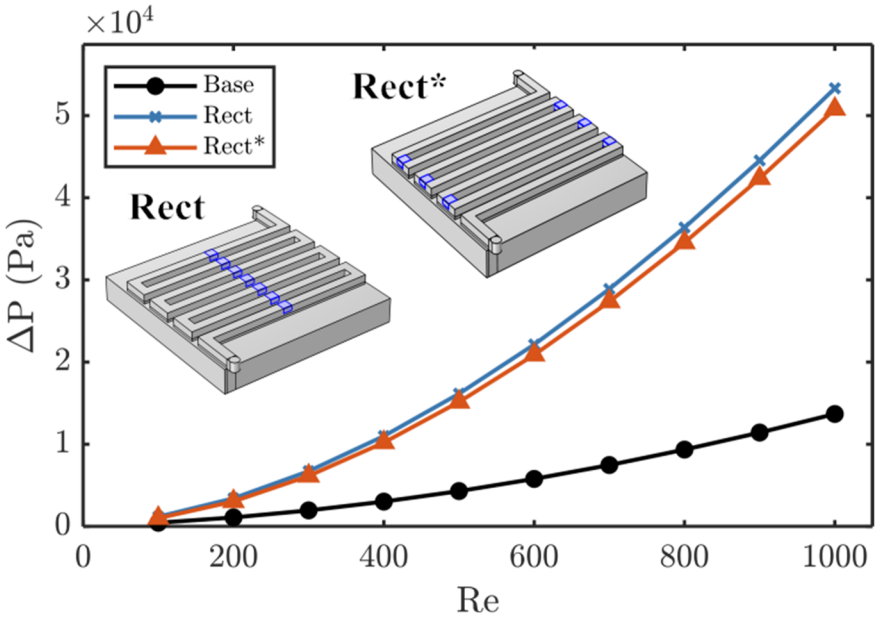

Figure 11. Pressure drop obtained for different obstacle positioning.

Figure 12c) compares the velocity flow fields between obstacles placed in straight vs. curved sections. When positioned in curved segments, obstacles exploit pre-existing low-velocity regions, leading to improved distribution across the electrode interface. These observations complement the

quantitative findings in Figure 12a),b) and align with previous studies [32], suggesting enhanced mixing and reactant penetration in such configurations.

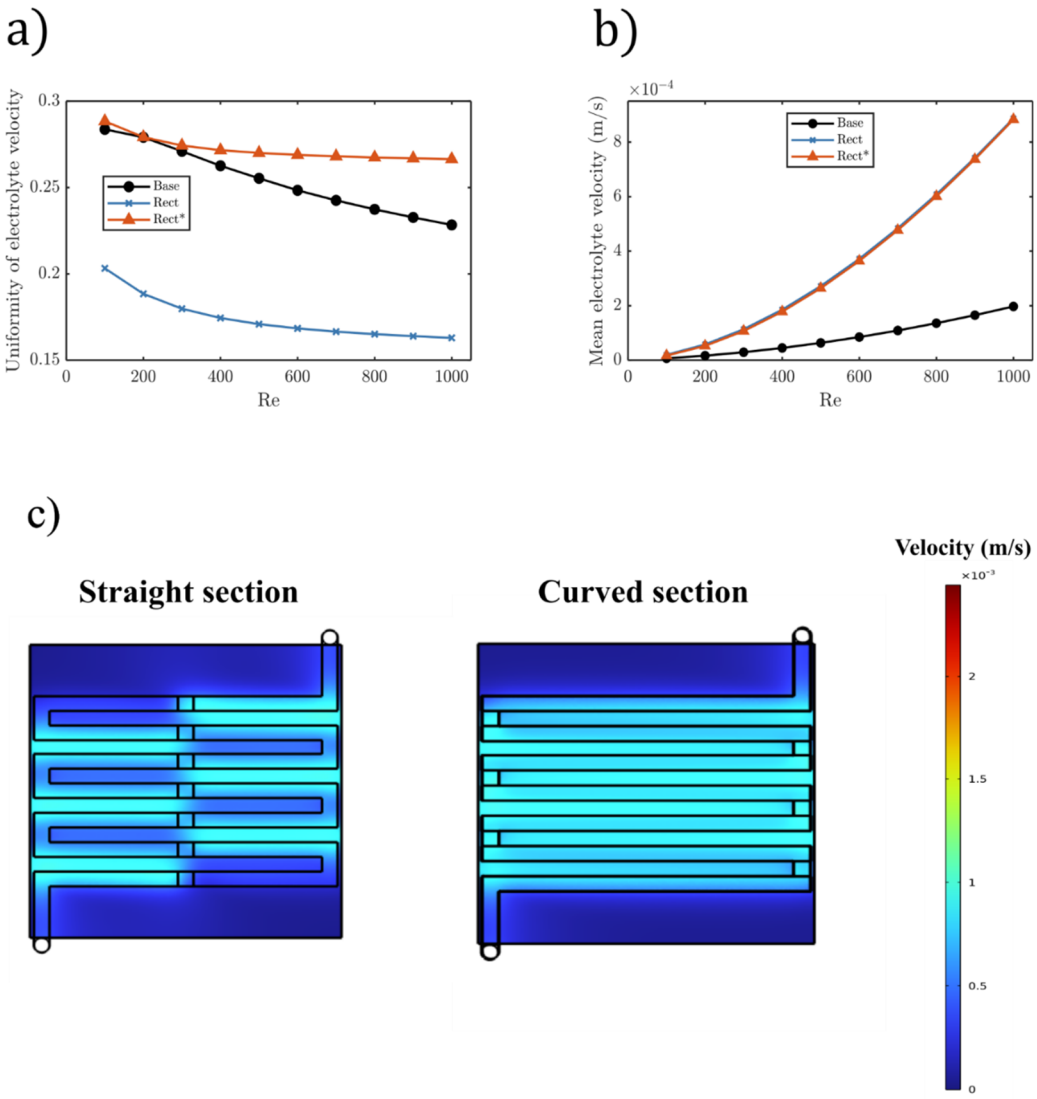

Figure 12. a) Uniformity of electrolyte velocity in the electrode, b) mean electrolyte velocity in the electrode, and c) velocity fields for different obstacle positioning for Re = 400.

3.6. Artificial neural network for pressure drop prediction

In the present study, a multilayer perceptron with backpropagation (MLP-BP) is employed for pressure drop prediction. The objective of using the neural network in this study is to create a surrogate model capable of rapidly predicting pressure drop for different obstacle configurations in the serpentine flow field. Once trained on data from 3D CFD simulations, the network enables fast and accurate estimations without the need for additional simulations. The MLP-BP is a type of artificial neural network (ANN) composed of layers of neurons, comprising an input layer, one or more hidden layers, and an output layer. Their versatility makes them a suitable alternative for modeling fluid dynamic systems, as in [33,34]. In this architecture, each neuron in a given layer is connected to every

neuron in the subsequent layer, and each connection is associated with a weight that determines its influence. The input data—defining the features of the case—are propagated through the network, with numerical computations performed layer by layer, until reaching the output layer, where target values are defined. In the case under study, 7 distinct inputs, a hidden layer with 14 neurons, and a single output were considered. Sigmoid activation functions are applied to the hidden layers, whereas a linear activation function is used in the output layer, which is suitable for regression tasks. The inputs were defined to fully characterize the case, comprising the number of sides of the obstacles, their height, width, and perimeter, the number of obstacles located on the straight and curved sections, and the inlet pressure. The output corresponds to the pressure drop. Figure 13 represents a schematic representation of the designed ANN. The Levenberg–Marquardt algorithm [35,36] with the mean squared error (MSE) loss function was used for training the network, and the dataset was split into 70% for training, 20% for validation, and 10% for testing. Training was conducted until validation loss reached its minimum value, before beginning to increase, in order to prevent overfitting. MATLAB 2025a [37] commercial code with its Deep Learning toolbox [38] was used to design and train the ANN.

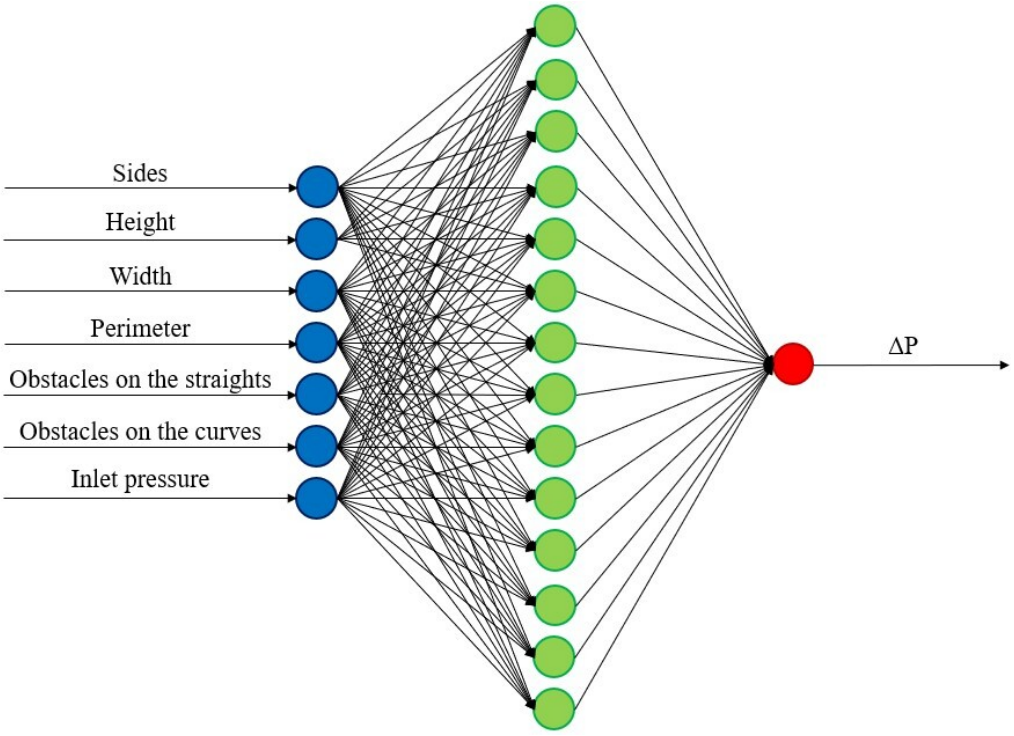

Figure 13. ANN for pressure drop prediction.

To evaluate the accuracy of the ANN predictions, the correlation coefficient (R-value) of the test set is considered, as these cases are unknown to the network, and thus assess the generalizability of the proposed model. Figure 14 presents the R-value results, which are equal to 0.99895, thereby demonstrating the high accuracy of the ANN predictions.

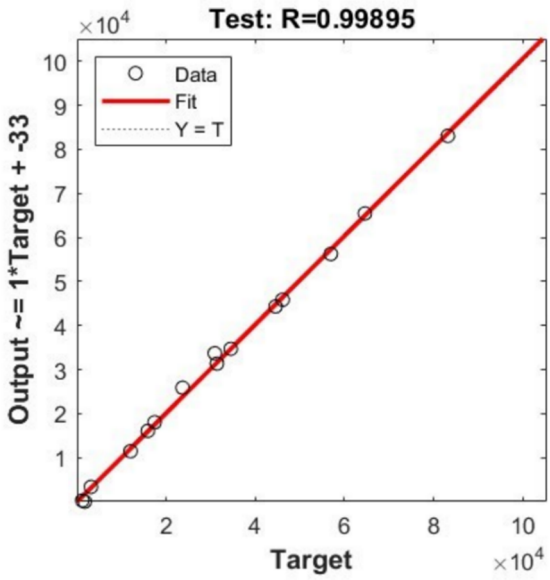

Figure 14. Correlation coefficient of the test set.

To further assess the performance of the neural network, Figure 15 presents a comparison between the ANN predictions for all considered obstacle configurations together with the CFD results. This comparison shows that the predictions provided by the ANN closely match the CFD values, accurately capturing the same trend.

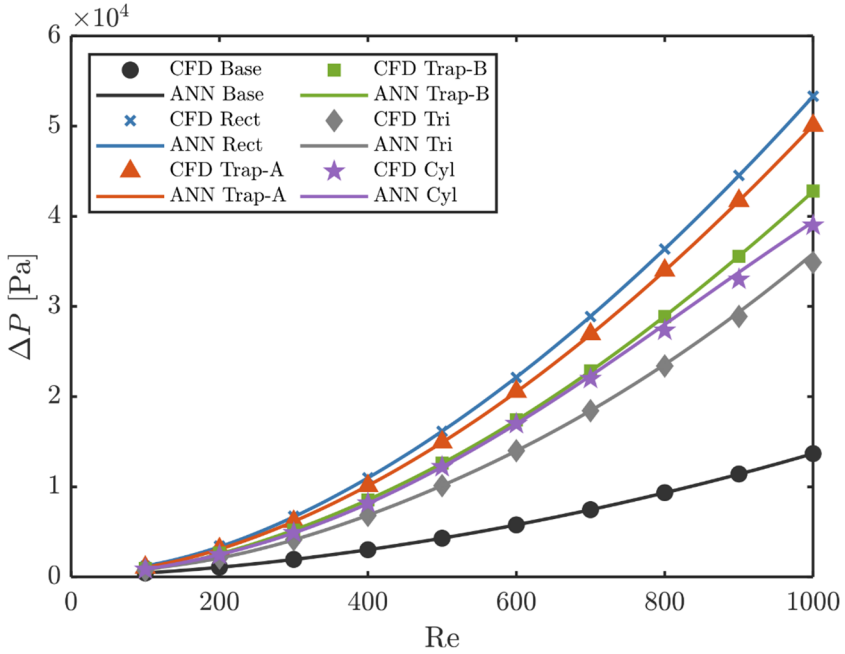

Figure 15. Comparison between the predictions of the ANN and the CFD results for all the considered obstacles.

Additionally, the ANN offers enhanced performance in terms of computational time, as obtaining a single prediction requires only $6 \cdot 10^{-4}$ s, whereas performing the CFD simulation of a single case requires 1000 s. This corresponds to a speed-up factor of $1.67 \cdot 10^{6}$ when compared to the performed CFD simulations.

4. Conclusions

This study investigated the impact of obstacle geometry, number, and placement within a serpentine flow field of a VRFB half-cell using a three-dimensional numerical model. The most important findings are summarized as follows:

- Among the tested geometries, the rectangular (*Rect*) obstacle yielded the highest mean electrolyte velocity but also had the largest pressure drop and lowest flow uniformity. In contrast, streamlined shapes such as cylindrical (*Cyl*) and trapezoidal (*Trap-B*) structures provided a better balance, improving velocity and maintaining uniformity with substantially lower hydraulic penalties.
- Increasing the number of obstacles from 1 to 3 significantly enhanced flow uniformity across all geometries, with the most notable gains occurring when increasing from 1 to 2 elements. *Trap-A* demonstrated efficient performance scaling, with its 2-block configuration reaching the same mean velocity as *Trap-B* with 3 blocks. The improvement rate diminished beyond 2 obstacles for all geometries.
- In terms of obstacle placement, introducing blocks into the curved section of the serpentine channel led to notable improvements (up to 9% over the *Base* case), with a negligible increase in pressure drop.
- With the performed simulations, an ANN-based model has been developed, which provides extremely fast and accurate predictions of the considered case, reducing the computational time required to obtain the results by 6 orders of magnitude. This approach could be employed in future work to efficiently explore alternative obstacle designs. Its rapid inference capability would allow for fast evaluation of multiple configurations without the need to generate new meshes and run additional CFD simulations, thereby facilitating broader parametric or optimization studies.

Use of AI tools declaration

The authors declare they have not used Artificial Intelligence (AI) tools in the creation of this article.

Acknowledgments

The authors are grateful for the support provided by SGIker of UPV/EHU. This research was developed under the frame of the Joint Research Laboratory on Offshore Renewable Energy (JRL-ORE). This work was partially supported by the Government of the Basque Country through the Elkartek HIDRURA - Tecnologías Innovadoras para la generación de Hidrógeno Verde program (Grant No.: KK-2024/00035) and the CIEMAT project "Energía eólica offshore para el ensayo y el desarrollo energético de energías renovables e hidrógeno verde". U. F. G. and E. Z. received support from the Mobility Lab Foundation, a governmental organization of the Provincial Council of Araba and the local council of Vitoria-Gasteiz. The assistance of the ITSAS-REM (IT1514-22) research team is also appreciated.

Conflict of interest

Unai Fernandez-Gamiz is a guest editor for the special issue of the ERA and was not involved in the editorial review or the decision to publish this article. All authors declare that there are no competing interests.

References

1. A. A. Kadhem, N. I. A. Wahab, I. Aris, J. Jasni, A. N. Abdalla, Y. Matsukawa, Reliability assessment of generating systems with wind power penetration via BPSO, *Int. J. Adv. Sci., Eng. Inf. Technol.*, **7** (2017), 1248–1254. https://doi.org/10.18517/ijaseit.7.4.2311
2. O. Smith, O. Cattell, E. Farcot, R. D. O'Dea, K. I. Hopcraft, The effect of renewable energy incorporation on power grid stability and resilience, *Sci. Adv.*, **8** (2022), eabj6734. https://doi.org/10.1126/sciadv.abj6734
3. T. S. Le, T. N. Nguyen, D. K. Bui, T. D. Ngo, Optimal sizing of renewable energy storage: A techno-economic analysis of hydrogen, battery and hybrid systems considering degradation and seasonal storage, *Appl. Energy*, **336** (2023), 120817. https://doi.org/10.1016/j.apenergy.2023.120817
4. M. O. Bamgbopa, A. Fetyan, M. Vagin, A. A. Adelodun, Towards eco-friendly redox flow batteries with all bio-sourced cell components, *J. Energy Storage*, **50** (2022), 104352. https://doi.org/10.1016/j.est.2022.104352
5. Z. Huang, A. Mu, L. Wu, B. Yang, Y. Qian, J. Wang, Comprehensive Analysis of Critical Issues in All-Vanadium Redox Flow Battery, *ACS Sustainable Chem. Eng.*, **10** (2022), 7786–7810. https://doi.org/10.1021/acssuschemeng.2c01372
6. A. Aluko, A. Knight, A review on vanadium redox flow battery storage systems for large-scale power systems application, *IEEE Access*, **11** (2023), 13773–13793. https://doi.org/10.1109/ACCESS.2023.3243800
7. K. Lourenssen, J. Williams, F. Ahmadpour, R. Clemmer, S. Tasnim, Vanadium redox flow batteries: A comprehensive review, *J. Energy Storage*, **25** (2019), 100844. https://doi.org/10.1016/j.est.2019.100844
8. K. Knehr, E. Agar, C. Dennison, A. Kalidindi, E. Kumbur, A transient vanadium flow battery model incorporating vanadium crossover and water transport through the membrane, *J. Electrochem. Soc.*, **159** (2012), A1446–A1459. https://doi.org/10.1149/2.017209jes
9. W. M. Carvalho, L. Cassayre, D. Quaranta, F. Chauvet, R. El-Hage, T. Tzedakis, et al., Stability of highly supersaturated vanadium electrolyte solution and characterization of precipitated phases for vanadium redox flow battery, *J. Energy Chem.*, **61** (2021), 436–445. https://doi.org/10.1016/j.jechem.2021.01.040
10. F. Rahman, M. Skyllas-Kazacos, Vanadium redox battery: Positive half-cell electrolyte studies, *J. Power Sources*, **189** (2009), 1212–1219. https://doi.org/10.1016/j.jpowsour.2008.12.113
11. S. Maurya, P. T. Nguyen, Y. S. Kim, Q. Kang, R. Mukundan, Effect of flow field geometry on operating current density, capacity and performance of vanadium redox flow battery, *J. Power Sources*, **404** (2018), 20–27. https://doi.org/10.1016/j.jpowsour.2018.09.093
12. Z. Huang, A. Mu, Flow field design and performance analysis of vanadium redox flow battery, *Ionics*, **27** (2021), 5207–5218. https://doi.org/10.1007/s11581-021-04213-8

13. J. Wang, A. Mu, B. Yang, W. Wang, Y. Wang, Enhancing vanadium flow battery performance via trapezoidal channel design: An experimental validation and parametric investigation, *J. Energy Storage*, **119** (2025), 116346. https://doi.org/10.1016/j.est.2025.116346
14. J. Ramesh, M. Premalatha, D. R. Sudhakar, G. A. Pathanjali, M. Raja, A novel flow design to reduce pressure drop and enhance performance of Vanadium Redox Flow Battery, *J. Energy Storage*, **108** (2025), 115030. https://doi.org/10.1016/j.est.2024.115030
15. Z. Huang, A. Mu, L. Wu, H. Wang, Vanadium redox flow batteries: Flow field design and flow rate optimization, *J. Energy Storage*, **45** (2022), 103526. https://doi.org/10.1016/j.est.2021.103526
16. M. Messaggi, P. Canzi, R. Mereu, A. Baricci, F. Inzoli, A. Casalegno, et al., Analysis of flow field design on vanadium redox flow battery performance: Development of 3D computational fluid dynamic model and experimental validation, *Appl. Energy*, **228** (2018), 1057–1070. https://doi.org/10.1016/j.apenergy.2018.06.148
17. Q. Xu, T. S. Zhao, C. Zhang, Performance of a vanadium redox flow battery with and without flow fields, *Electrochim. Acta*, **142** (2014), 61–67. https://doi.org/10.1016/j.electacta.2014.07.059
18. Y. Wang, M. Li, L. Hao, Three-dimensional modeling study of all-vanadium redox flow batteries with the serpentine and interdigitated flow fields, *J. Electroanal. Chem.*, **918** (2022), 116460. https://doi.org/10.1016/j.jelechem.2022.116460
19. M. Yue, Q. Zheng, F. Xing, H. Zhang, X. Li, X. Ma, Flow field design and optimization of high power density vanadium flow batteries: A novel trapezoid flow battery, *AIChE J.*, **64** (2018), 782–795. https://doi.org/10.1002/aic.15959
20. J. Lee, J. Kim, H. Park, Numerical simulation of the power-based efficiency in vanadium redox flow battery with different serpentine channel size, *Int. J. Hydrogen Energy*, **44** (2019), 29483–29492. https://doi.org/10.1016/j.ijhydene.2019.05.013
21. E. Ali, J. Kim, H. Park, Numerical analysis of modified channel widths of serpentine and interdigitated channels for the discharge performance of vanadium redox flow batteries, *J. Energy Storage*, **53** (2022), 105099. https://doi.org/10.1016/j.est.2022.105099
22. R. Gundlapalli, S. Jayanti, Effect of channel dimensions of serpentine flow fields on the performance of a vanadium redox flow battery, *J. Energy Storage*, **23** (2019), 148–158. https://doi.org/10.1016/j.est.2019.03.014
23. J. Sun, B. Liu, M. Zheng, Y. Luo, Z. Yu, Serpentine flow field with changing rib width for enhancing electrolyte penetration uniformity in redox flow batteries, *J. Energy Storage*, **49** (2022), 104135. https://doi.org/10.1016/j.est.2022.104135
24. Z. Guo, J. Sun, X. Fan, T. Zhao, Numerical modeling of a convection-enhanced flow field for high-performance redox flow batteries, *J. Power Sources*, **583** (2023), 233540. https://doi.org/10.1016/j.jpowsour.2023.233540
25. Z. Huang, A. Mu, L. Wu, H. Wang, Y. Zhang, Electrolyte flow optimization and performance metrics analysis of vanadium redox flow battery for large-scale stationary energy storage, *Int. J. Hydrogen Energy*, **46** (2021), 31952–31962. https://doi.org/10.1016/j.ijhydene.2021.06.220
26. L. Pan, J. Sun, H. Qi, M. Han, L. Chen, J. Xu, et al., Along-flow-path gradient flow field enabling uniform distributions of reactants for redox flow batteries, *J. Power Sources*, **570** (2023), 233012. https://doi.org/10.1016/j.jpowsour.2023.233012
27. B. Akuzum, Y. C. Alparslan, N. C. Robinson, E. Agar, E. C. Kumbur, Obstructed flow field designs for improved performance in vanadium redox flow batteries, *J. Appl. Electrochem.*, **49** (2019), 551–561. https://doi.org/10.1007/s10800-019-01306-1

28. M. Messaggi, C. Gambaro, A. Casalegno, M. Zago, Development of innovative flow fields in a vanadium redox flow battery: Design of channel obstructions with the aid of 3D computational fluid dynamic model and experimental validation through locally-resolved polarization curves, *J. Power Sources*, **526** (2022), 231155. https://doi.org/10.1016/j.jpowsour.2022.231155
29. Y. Liu, Z. Huang, X. Xie, Y. Liu, J. Wu, Z. Guo, et al., Redox flow battery: Flow field design based on bionic mechanism with different obstructions, *Chem. Eng. J.*, **498** (2024), 155663. https://doi.org/10.1016/j.cej.2024.155663
30. J. Martínez-López, U. Fernández-Gamiz, E. Sánchez-Díez, A. Beloki-Arrondo, Í. Ortega-Fernández, Enhancing mass transport in organic redox flow batteries through electrode obstacle design, *Batteries*, **11** (2025). https://doi.org/10.3390/batteries11010029
31. Q. Wang, Z. G. Qu, Z. Y. Jiang, W. W. Yang, Experimental study on the performance of a vanadium redox flow battery with non-uniformly compressed carbon felt electrode, *Appl. Energy*, **213** (2018), 293–305. https://doi.org/10.1016/j.apenergy.2018.01.047
32. M. Y. Lu, Y. H. Jiao, X. Y. Tang, W. W. Yang, M. Ye, Q. Xu, Blocked serpentine flow field with enhanced species transport and improved flow distribution for vanadium redox flow battery, *J. Energy Storage*, **35** (2021), 102284. https://doi.org/10.1016/j.est.2021.102284
33. K. Portal-Porras, U. Fernandez-Gamiz, E. Zulueta, R. Garcia-Fernandez, O. Irigaray, Parametric study of vortex generators on a fin-and-tube heat exchanger, *Energy Sources, Part A*, **45** (2023), 10051–10072. https://doi.org/10.1080/15567036.2023.2242809
34. J. Martínez-López, K. Portal-Porras, U. Fernández-Gamiz, E. Sánchez-Díez, J. Olarte, I. Jonsson, Voltage and overpotential prediction of vanadium redox flow batteries with artificial neural networks, *Batteries*, **10** (2024). https://doi.org/10.3390/batteries10010023
35. M. T. Hagan, M. B. Menhaj, Training feedforward networks with the Marquardt algorithm, *IEEE Trans. Neural Networks*, **5** (1994), 989–993. https://doi.org/10.1109/72.329697
36. B. G. Kermani, S. S. Schiffman, H. T. Nagle, Performance of the Levenberg–Marquardt neural network training method in electronic nose applications, *Sens. Actuators, B*, **110** (2005), 13–22. https://doi.org/10.1016/j.snb.2005.01.008
37. *MATLAB*, 2025. Available from: https://www.mathworks.com/products/matlab.html.
38. *Deep Learning Toolbox,* 2025. Available from: https://www.mathworks.com/products/deep-learning.html.